

Stable Reconstruction of Anisotropic Objects from Near-Field Electromagnetic Data

Tran H. Lan* Dinh-Liem Nguyen[†]

Abstract

This paper addresses the electromagnetic inverse scattering problem of determining the location and shape of anisotropic objects from near-field data. We investigate both cases involving the Helmholtz equation and Maxwell's equations for this inverse problem. Our study focuses on developing efficient imaging functionals that enable a fast and stable recovery of the anisotropic object. The implementation of the imaging functionals is simple and avoids the need to solve an ill-posed problem. The resolution analysis of the imaging functionals is conducted using the Green representation formula. Furthermore, we establish stability estimates for these imaging functionals when noise is present in the data. To illustrate the effectiveness of the methods, we present numerical examples showcasing their performance.

Keywords. stable imaging functional, electromagnetic inverse scattering, near-field data, Maxwell's equations

AMS subject classification. 35R30, 35R09, 65R20

1 Introduction

We consider the inverse scattering problem for both the Helmholtz equation and Maxwell's equations concerning anisotropic objects. This inverse problem has important applications in various areas including nondestructive testing, radar imaging, medical imaging, and geophysical exploration [8]. There has been a substantial body of literature on both theoretical and numerical investigations of this inverse problem and its variants, see [4, 8] and references therein. For numerical solving of the inverse problem, sampling methods (e.g. linear sampling method [7], factorization method [17]) offer distinct advantages over nonlinear optimization-based techniques. These sampling methods are fast, non-iterative and do not require advanced a priori information about the unknown target. More details about sampling methods can be found in [3, 5, 6, 20, 26] and references therein.

*Faculty of Applied Sciences, Ho Chi Minh City University of Technology and Education, Ho Chi Minh City, Vietnam; (lanth@hcmute.edu.vn)

[†]Department of Mathematics, Kansas State University, Manhattan, KS 66506, USA; (dlnghuyen@ksu.edu)

The work in this paper is inspired by the orthogonality sampling method (OSM) proposed in [27]. This method is also studied in other works under the name of direct sampling method. While inheriting the advantages of the aforementioned classical sampling methods (e.g. [7,17]), the OSM is attractive and promising thanks to its simplicity and efficiency. More precisely, the OSM is very robust against noise in the data, its stability is easily justified, its implementation is simple and avoids the need to solve an ill-posed problem. However, the theoretical analysis of the OSM is far less developed compared with that of the classical sampling methods. The majority of the published results concerns the case of far-field measurements, see [1, 9, 10, 13, 14, 23, 25, 27] for some results on the scalar Helmholtz equation and [11, 15, 16, 22, 24] for results on the Maxwell's equations.

The results on the OSM concerning the case of near-field measurements are limited. The OSM studied in [2] is specifically applicable to the 2D case with circular measurement boundaries. The 3D case was studied in [16] under the small volume hypothesis of well-separated inhomogeneities. The imaging functionals introduced in this paper, along with their associated analysis, are not confined to small scatterers or circular measurement boundaries. Nevertheless, they do require Cauchy data rather than solely relying on scattered field data. An imaging functional using near-field Cauchy data was studied in [12] for anisotropic objects. This functional is related to our imaging functional studied in the scalar case, but its resolution analysis requires that the material parameter of the scattering object must be smooth. Additionally, instead of using the Green's function as in [12] we only employ the imaginary part of the Green's function in the imaging functional. This approach helps avoid dealing the blow-up singularity of the Green's function when the boundary of the sampling domain approaches the measurement boundary.

The use of near-field Cauchy data was also studied in [21] in the context of the isotropic Helmholtz equation with data generated by a single incident wave. This paper can be seen as an extended study of the findings in [21] to the cases of the anisotropic Helmholtz equation and Maxwell's equations. The latter cases are technically more complex than the isotropic Helmholtz equation case demanding a meticulous analysis of the resolution and stability of the imaging functional. Additionally, it's worth noting that, for the case of Maxwell's equations, we suggest using several polarization vectors, denoted by \mathbf{p}_n , involved in the imaging functional that notably improve the reconstruction results. Our resolution analysis of the imaging functional is based on the integro-differential equation representation of the scattered field and the Green representation formula of the imaginary part of the Green's function (or tensor) of the direct scattering problem. We show that the imaging functional can be expressed as a functional that involves Bessel functions $J_0(k|y-z|)$ or $j_0(k|y-z|)$ and their derivatives where z is a sampling point and y is a point inside the unknown scatterer. These Bessel functions are crucial for justifying the behavior of the imaging functional. Furthermore, we establish stability estimates for these imaging functionals when noise is present in the near-field scattering data. Finally, we illustrate the effectiveness of the methods with numerical examples in both 2D and 3D.

The rest of the paper is organized as follows. The second section includes the study of the Helmholtz equation case where we formulate the inverse problem of interest, introduce the imaging functional, analyze its behavior, and showcase numerical examples. Section 3 is

dedicated to the case of Maxwell's equations with a structure that is similar to that of the scalar case.

2 The Helmholtz Equation Case

We first formulate the inverse problem of interest. Consider a penetrable inhomogeneous medium that occupies a bounded Lipschitz domain $D \subset \mathbb{R}^n$ ($n = 2$ or 3). Assume that this medium is characterized by the bounded matrix-valued ($n \times n$ matrix) function Q and that $Q = 0I_n$ in $\mathbb{R}^n \setminus \overline{D}$, where I_n is the $n \times n$ identity matrix. Consider the incident plane wave

$$u_{\text{in}}(x, d) = e^{ikx \cdot d}, \quad x \in \mathbb{R}^n, \quad d \in \mathbb{S}^{n-1} := \{x \in \mathbb{R}^n : |x| = 1\},$$

where $k > 0$ is the wave number and d is the direction vector of propagation. We note that point sources can also be employed as incident waves without affecting the analysis of the reconstruction method studied in this paper. We consider the following model problem for the scattering of $u_{\text{in}}(x, d)$ by the inhomogeneous anisotropic medium

$$\operatorname{div}((I_n + Q)\nabla u) + k^2 u = 0, \quad x \in \mathbb{R}^n, \quad (1)$$

$$u = u_{\text{sc}} + u_{\text{in}}, \quad (2)$$

$$\lim_{r \rightarrow \infty} r^{\frac{n-1}{2}} \left(\frac{\partial u_{\text{sc}}}{\partial r} - ik u_{\text{sc}} \right) = 0, \quad r = |x|, \quad (3)$$

where $u(x, d)$ is the total field, $u_{\text{sc}}(x, d)$ is the scattered field, and the Sommerfeld radiation condition (3) holds uniformly for all directions $x/|x| \in \mathbb{S}^{n-1}$. We refer to [19] for the well-posedness of this scattering problem. For the study of the inverse problem discussed below we assume that the direct problems is well-posed.

Consider a regular domain $\Omega \subset \mathbb{R}^n$ such that $\overline{D} \subset \Omega$ and denote by $\nu(x)$ the outward normal unit vector to $\partial\Omega$ at x .

Inverse problem. Given $u_{\text{sc}}(\cdot, d_j)$ and $\partial u_{\text{sc}}(\cdot, d_j)/\nu$ on $\partial\Omega$ for $d_j \in \mathbb{S}^{n-1}$ where $j = 1, 2, \dots, N$, determine D .

We denote by $\Phi(x, y)$ the free-space Green's function of the scattering problem (1)–(3). It is well known that

$$\Phi(x, y) = \begin{cases} \frac{i}{4} H_0^{(1)}(k|x-y|), & \text{in } \mathbb{R}^2, \\ \frac{e^{ik|x-y|}}{4\pi|x-y|}, & \text{in } \mathbb{R}^3. \end{cases} \quad (4)$$

It is also known from [19] that the scattered wave u_{sc} (weak solution in $H_{\text{loc}}^1(\mathbb{R}^n)$) of problem (1)–(3) can be described by the following integro-differential equation

$$u_{\text{sc}}(x) = \operatorname{div}_x \int_D \Phi(x, y) Q(y) \nabla u(y) dy, \quad x \in \mathbb{R}^n. \quad (5)$$

This integro-differential equation formulation for the scattered wave u_{sc} is important to the study of the imaging functional in the next section.

2.1 Stable Imaging Functional

In this section we introduce the imaging functional and analyze its properties. This functional was introduced in [21] for the case of the isotropic Helmholtz equation with data generated by a single incident wave. For the case of data generated by multiple incident waves we define the imaging functional $I(z)$ as

$$I(z) := \sum_{j=1}^N \left| \int_{\partial\Omega} u_{\text{sc}}(x, d_j) \frac{\partial \text{Im} \Phi(x, z)}{\partial \nu(x)} - \frac{\partial u_{\text{sc}}(x, d_j)}{\partial \nu(x)} \text{Im} \Phi(x, z) \text{d}s(x) \right|^p, \quad (6)$$

where $p \in \mathbb{N}$ is used to sharpen the significant peaks of $I(z)$.

Recall that J_0 and j_0 are respectively a Bessel function and a spherical Bessel function of the first kind. The behavior of $I(z)$ is analyzed in the following theorem.

Theorem 1. *The imaging functional $I(z)$ satisfies*

$$I(z) := \sum_{j=1}^N \left| \int_D \mathcal{K}(y, z) \cdot Q(y) \nabla u(y, d_j) \text{d}y \right|^p, \quad (7)$$

where

$$\mathcal{K}(y, z) = \begin{cases} \frac{1}{4} \nabla_y J_0(k|y - z|), & \text{in } \mathbb{R}^2, \\ \frac{k}{4\pi} \nabla_y j_0(k|y - z|), & \text{in } \mathbb{R}^3. \end{cases}$$

Furthermore

$$I(z) = O\left(\frac{1}{\text{dist}(z, D)^{\frac{p(n-1)}{2}}}\right) \quad \text{as } \text{dist}(z, D) \rightarrow \infty, \quad (8)$$

where $\text{dist}(z, D)$ is the distance from z to D .

Remark 2. *For a fixed y in \mathbb{R}^2 , we observe that while $|\partial_{y_1} J_0(k|y - z|)|^2$, $|\partial_{y_2} J_0(k|y - z|)|^2$, and $|\nabla_y J_0(k|y - z|)|^2$ do not exhibit peaks at $z = y$, they do have relatively larger magnitudes in a small neighborhood near y . As z is away from y these magnitudes decay quickly, as illustrated in Figure 1. Especially the peaks near y are sharper and stronger for higher values of k . Thus for an extended object D , according to Theorem 1, we anticipate that the imaging functional $I(z)$ (with, e.g., $p = 2$) will attain higher values when z belongs to D , while $I(z)$ will be considerably smaller when z lies outside D . This is indeed confirmed in the numerical study.*

Proof. For the sake of simplicity in presentation, we omit the dependence of the total wave u on d_j . From the integro-differential equation (5) and through a direct calculation we derive

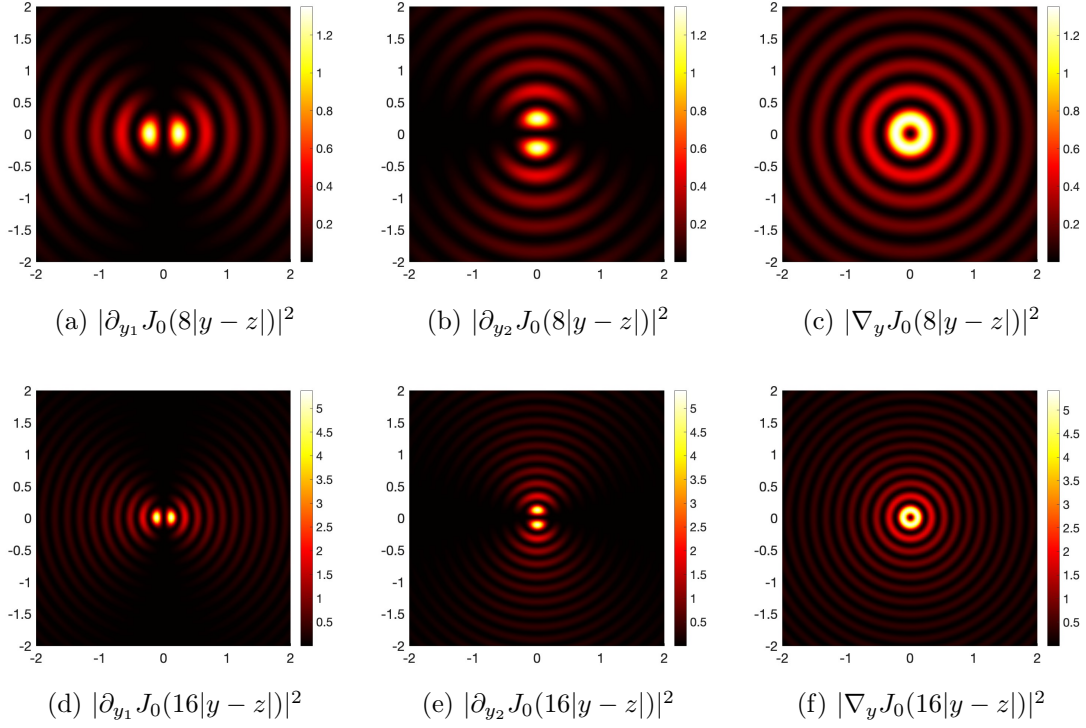


Figure 1: Plots illustrating each component and the modulus of the 2D kernel $\mathcal{K}(y, z)$ for $y = 0$, $z \in (-2, 2)^2$, $k = 8$, and $k = 16$. First row (a, b, c): plots of $|\partial_{y_1} J_0(k|y - z)|^2$, $|\partial_{y_2} J_0(k|y - z)|^2$ and $|\nabla_y J_0(k|y - z)|^2$ for $k = 8$. Second row (d, e, f): plots of $|\partial_{y_1} J_0(k|y - z)|^2$, $|\partial_{y_2} J_0(k|y - z)|^2$ and $|\nabla_y J_0(k|y - z)|^2$ for $k = 16$.

that

$$\begin{aligned}
& \int_{\partial\Omega} \left(\frac{\partial \text{Im } \Phi(x, z)}{\partial \nu(x)} u_{\text{sc}}(x) - \text{Im } \Phi(x, z) \frac{\partial u_{\text{sc}}(x)}{\partial \nu(x)} \right) ds(x) \\
&= \int_{\partial\Omega} \left(\frac{\partial \text{Im } \Phi(x, z)}{\partial \nu(x)} \text{div}_x \int_D \Phi(x, y) Q(y) \nabla u(y) dy \right. \\
&\quad \left. - \text{Im } \Phi(x, z) \frac{\partial}{\partial \nu(x)} \text{div}_x \int_D \Phi(x, y) Q(y) \nabla u(y) dy \right) ds(x) \\
&= \int_{\partial\Omega} \left(\frac{\partial \text{Im } \Phi(x, z)}{\partial \nu(x)} \int_D \nabla_x \Phi(x, y) \cdot Q(y) \nabla u(y) dy \right. \\
&\quad \left. - \text{Im } \Phi(x, z) \frac{\partial}{\partial \nu(x)} \int_D \nabla_x \Phi(x, y) \cdot Q(y) \nabla u(y) dy \right) ds(x).
\end{aligned}$$

Now exchanging the integrals and employing the fact that $\nabla_x \Phi(x, y) = -\nabla_y \Phi(x, y)$ we derive

$$\begin{aligned} & \int_{\partial\Omega} \left(\frac{\partial \operatorname{Im} \Phi(x, z)}{\partial \nu(x)} u_{\text{sc}}(x) - \operatorname{Im} \Phi(x, z) \frac{\partial u_{\text{sc}}(x)}{\partial \nu(x)} \right) ds(x) \\ &= - \int_D \nabla_y \int_{\partial\Omega} \left(\frac{\partial \operatorname{Im} \Phi(x, z)}{\partial \nu(x)} \Phi(y, x) - \operatorname{Im} \Phi(x, z) \frac{\partial \Phi(y, x)}{\partial \nu(x)} \right) ds(x) \cdot Q(y) \nabla u(y) dy. \end{aligned} \quad (9)$$

It is known (see [8]) that for all $z, y \in \mathbb{R}^n$

$$\Delta \operatorname{Im} \Phi(z, y) + k^2 \operatorname{Im} \Phi(z, y) = 0.$$

Hence, we deduce from the Green representation formula that

$$\int_{\partial\Omega} \left(\frac{\partial \operatorname{Im} \Phi(x, z)}{\partial \nu(x)} \Phi(y, x) - \operatorname{Im} \Phi(x, z) \frac{\partial \Phi(y, x)}{\partial \nu(x)} \right) ds(x) = \operatorname{Im} \Phi(y, z).$$

Therefore, substituting this identity in (9) implies

$$\int_{\partial\Omega} \left(\frac{\partial \operatorname{Im} \Phi(x, z)}{\partial \nu(x)} u_{\text{sc}}(x) - \operatorname{Im} \Phi(x, z) \frac{\partial u_{\text{sc}}(x)}{\partial \nu(x)} \right) ds(x) = - \int_D \nabla_y \operatorname{Im} \Phi(y, z) \cdot Q(y) \nabla u(y) dy.$$

Replacing this equation in (6) and letting $\mathcal{K}(y, z) = \nabla_y \operatorname{Im} \Phi(y, z)$ we derive (7).

Now we justify (8) for the two-dimensional case. First we have

$$\nabla_y J_0(k|y - z|) = -k \left(\frac{(y_1 - z_1)}{|y - z|}, \frac{(y_2 - z_2)}{|y - z|} \right)^\top J_1(k|y - z|),$$

where J_1 is a Bessel function of the first kind and first order. Using this and the Cauchy-Schwartz inequality we obtain

$$\left| \int_D \nabla_y J_0(k|y - z|) \cdot Q(y) \nabla u(y, d_j) dy \right|^p \leq \|k J_1(k|\cdot - z|)\|^p \|Q \nabla u(\cdot, d_j)\|^p$$

Now (8) will follow from the well-known asymptotic behavior of J_1

$$J_1(k|y - z|) = O \left(\frac{1}{\sqrt{|y - z|}} \right), \quad \text{as } |y - z| \rightarrow \infty.$$

The three-dimensional case can be done similarly. \square

In practice the data are always perturbed with some noise. We assume the noisy data u_{sc}^δ and $\partial u_{\text{sc}}^\delta / \partial \nu$ satisfy

$$\sum_{j=1}^N \|u_{\text{sc}}(\cdot, d_j) - u_{\text{sc}}^\delta(\cdot, d_j)\|_{L^2(\partial\Omega)} \leq \delta_1, \quad (10)$$

$$\sum_{j=1}^N \left\| \frac{\partial u_{\text{sc}}(\cdot, d_j)}{\partial \nu} - \frac{\partial u_{\text{sc}}^\delta(\cdot, d_j)}{\partial \nu} \right\|_{L^2(\partial\Omega)} \leq \delta_2, \quad (11)$$

for some positive constants δ_1 and δ_2 . We now prove a stability estimate for the imaging functional $I(z)$.

Theorem 3. Denote by $I^\delta(z)$ the imaging functional corresponding to noisy data u_{sc}^δ and $\partial u_{\text{sc}}^\delta/\partial\nu$, i.e.

$$I^\delta(z) := \sum_{j=1}^N \left| \int_{\partial\Omega} u_{\text{sc}}^\delta(x, d_j) \frac{\partial \text{Im} \Phi(x, z)}{\partial\nu(x)} - \frac{\partial u_{\text{sc}}^\delta(x, d_j)}{\partial\nu(x)} \text{Im} \Phi(x, z) ds(x) \right|^p.$$

Then for all $z \in \mathbb{R}^3$,

$$|I(z) - I^\delta(z)| = O(\max\{\delta_1, \delta_2\}) \quad \text{as } \max\{\delta_1, \delta_2\} \rightarrow 0.$$

Proof. For $j = 1, 2, \dots, N$, we denote by

$$\begin{aligned} \alpha_j &= \left| \int_{\partial\Omega} u_{\text{sc}}(x, d_j) \frac{\partial \text{Im} \Phi(x, z)}{\partial\nu(x)} - \frac{\partial u_{\text{sc}}(x, d_j)}{\partial\nu(x)} \text{Im} \Phi(x, z) ds(x) \right|, \\ \beta_j &= \left| \int_{\partial\Omega} u_{\text{sc}}^\delta(x, d_j) \frac{\partial \text{Im} \Phi(x, z)}{\partial\nu(x)} - \frac{\partial u_{\text{sc}}^\delta(x, d_j)}{\partial\nu(x)} \text{Im} \Phi(x, z) ds(x) \right|. \end{aligned}$$

Then using the triangle and Cauchy-Schwarz inequalities and (10)-(11) we estimate that

$$\begin{aligned} |\alpha_j - \beta_j| &\leq \left\| \frac{\partial \text{Im} \Phi(\cdot, z)}{\partial\nu} \right\| \|u_{\text{sc}}(\cdot, d_j) - u_{\text{sc}}^\delta(\cdot, d_j)\| + \|\text{Im} \Phi(\cdot, z)\| \left\| \frac{\partial u_{\text{sc}}(\cdot, d_j)}{\partial\nu} - \frac{\partial u_{\text{sc}}^\delta(\cdot, d_j)}{\partial\nu} \right\| \\ &\leq \sqrt{\left\| \frac{\partial \text{Im} \Phi(\cdot, z)}{\partial\nu} \right\|^2 + \|\text{Im} \Phi(\cdot, z)\|^2} \max\{\delta_1, \delta_2\}. \end{aligned}$$

For the convenience of the presentation we always use C as a generic constant. With the help of the estimate above for $|\alpha_j - \beta_j|$ and the triangle inequality we have that

$$\begin{aligned} |I^\delta(z) - I(z)| &\leq \sum_{j=1}^N |\beta_j^p - \alpha_j^p| \leq \left(\sum_{j=1}^N |\beta_j - \alpha_j| \right) \left(\sum_{l=1}^N \left| \sum_{m=0}^{p-1} \beta_j^m \alpha_j^{p-1-m} \right| \right) \\ &\leq C \max\{\delta_1, \delta_2\} \sum_{j=1}^N \sum_{m=0}^{p-1} (|\beta_j - \alpha_j| + \alpha_j)^m \alpha_j^{p-1-m}. \end{aligned}$$

Then denoting $\alpha_{\max} = \max_{j=1, \dots, N} \alpha_j$ and using the estimate $(a+b)^m \leq 2^m(a^m + b^m)$ for nonnegative numbers a, b and $m = 0, \dots, p-1$ we continue to estimate that

$$\begin{aligned} |I^\delta(z) - I(z)| &\leq C \max\{\delta_1, \delta_2\} \sum_{j=1}^N \sum_{m=0}^{p-1} 2^m (|\beta_j - \alpha_j|^m + \alpha_j^m) \alpha_j^{p-1-m} \\ &\leq C \max\{\delta_1, \delta_2\} \sum_{m=0}^{p-1} 2^m \alpha_{\max}^{p-1-m} \sum_{j=1}^N (|\beta_j - \alpha_j|^m + \alpha_{\max}^m) \\ &\leq C \max\{\delta_1, \delta_2\} \sum_{m=0}^{p-1} 2^m (C^m \max\{\delta_1, \delta_2\}^m \alpha_{\max}^{p-1-m} + N \alpha_{\max}^{p-1}) \\ &= O(\max\{\delta_1, \delta_2\}), \quad \text{as } \max\{\delta_1, \delta_2\} \rightarrow 0. \end{aligned}$$

This completes the proof. \square

Remark 4. *It is important to observe that if the far-field measurements are acquired along the boundary of a large-radius ball, utilizing the radiation condition allows us to approximate $\partial u_{\text{sc}}/\partial \nu$ by iku_{sc} within $I(z)$. Then the modified imaging functional*

$$I_{\text{far}}(z) := \sum_{j=1}^N \left| \int_{\partial\Omega} u_{\text{sc}}(x, d_j) \frac{\partial \text{Im } \Phi(x, z)}{\partial \nu(x)} - ik u_{\text{sc}}(x, d_j) \text{Im } \Phi(x, z) ds(x) \right|^p \quad (12)$$

only needs the scattered field data $u_{\text{sc}}(x, d)$ and approximates $I(z)$.

2.2 Numerical Examples

In this section we study the numerical performance of the imaging functional (6) for simulated data in two dimensions. More precisely, we will examine the performance of the functional for data with different wave numbers (Figure 2), different number of incident waves (Figure 3), and different powers p (Figure 4). To ensure a consistent comparison, the imaging functional is normalized by dividing it with its maximal value. Its value is thus between 0 and 1.

The following common parameters are used in the numerical examples

$$\begin{aligned} \partial\Omega &= \{(x_1, x_2)^\top \in \mathbb{R}^2 : x_1^2 + x_2^2 = 3^2\}, \\ \text{Number of data points on } \partial\Omega &: 64 \text{ (uniformly distributed)}, \\ \text{Sampling domain} &: (-2, 2) \times (-2, 2), \\ \text{Number of sampling points} &: 96 \times 96. \end{aligned}$$

The following scattering objects are considered in the numerical examples.

a) Kite-ellipse object

$$\begin{aligned} \text{kite} &= \{x \in \mathbb{R}^2 : x = ((\cos(t) + 0.65 \cos(2t) - 0.65)/2, 1.5 \sin(t)/2.5)^\top, 0 \leq t \leq 2\pi\}, \\ \text{ellip} &= \{(x_1, x_2)^\top \in \mathbb{R}^2 : (x_1 - 1)^2/0.4^2 + (x_2 + 0.75)^2/0.6^2 < 1\} \\ D &= \text{disk} \cup \text{rectangle}, \\ Q(x) &= \text{diag}(0.5, 0.7) \quad \text{in } D. \end{aligned}$$

b) Rectangle object

$$\begin{aligned} D &= \{(x_1, x_2)^\top \in \mathbb{R}^2 : |x_1 - 0.2| < 0.6, |x_2 - 0.2| < 0.6\}, \\ Q(x) &= \text{diag}(0.5, 0.7) \quad \text{in } D. \end{aligned}$$

Here for simplicity we consider Q as a diagonal matrix with constant entries in D . It's worth noting that the well-posedness of the direct problem (see [19]) requires that $Q + I_n$ is symmetric and positive definite. Using N incident plane waves and measuring the data at 64 points on $\partial\Omega$ for each incident wave, the Cauchy data $u_{\text{sc}}(x, d)$, $\partial u_{\text{sc}}/\partial \nu(x, d)$, where $(x, d) \in \partial\Omega \times \mathbb{S}$, are then $N \times 64$ matrices. The artificial noise is simulated as two complex-valued noise matrices $\mathcal{N}_{1,2}$ containing random numbers that are uniformly distributed in the complex square

$$\{a + ib : |a| \leq 1, |b| \leq 1\} \subset \mathbb{C}.$$

For simplicity we consider the same noise level δ for both u_{sc} and $\partial u_{\text{sc}}/\partial\nu$. The noisy data u_{sc}^δ and $\partial u_{\text{sc}}^\delta/\partial\nu$ are given by

$$u_{\text{sc}}^\delta := u_{\text{sc}} + \delta \frac{\mathcal{N}_1}{\|\mathcal{N}_1\|_F} \|u_{\text{sc}}\|_F, \quad \frac{\partial u_{\text{sc}}^\delta}{\partial\nu} := \frac{\partial u_{\text{sc}}}{\partial\nu} + \delta \frac{\mathcal{N}_2}{\|\mathcal{N}_2\|_F} \left\| \frac{\partial u_{\text{sc}}}{\partial\nu} \right\|_F,$$

where $\|\cdot\|_F$ is the Frobenius matrix norm.

2.2.1 Reconstruction with different wave numbers (Figure 2)

We present the reconstruction results in Figure 2 for the wave numbers $k = 8$ (wavelength ≈ 0.78) and $k = 16$ (wavelength ≈ 0.39). For the data, we use 32 incident waves and introduce 2% noise ($\delta = 0.02$). This example intentionally employs a small amount of noise in the data to distinctly display the impact of using different wave numbers in the reconstruction process. Figure 2 illustrates that the reconstruction results notably improve with higher values of k .

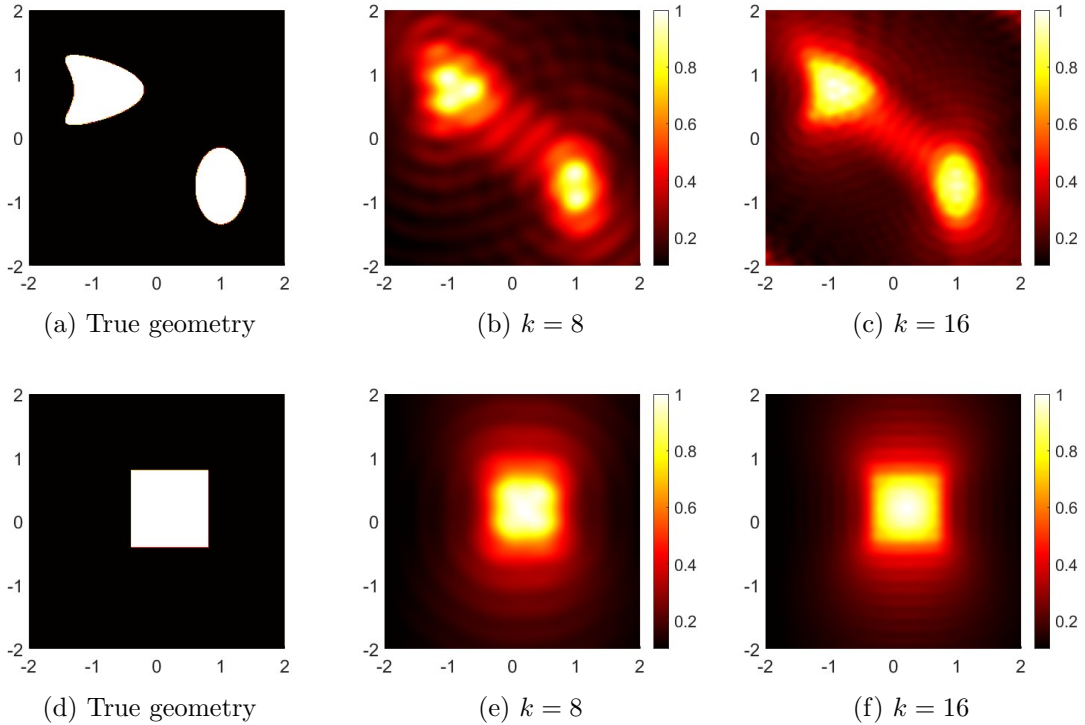


Figure 2: Reconstruction from data associated with different wave numbers. The data is generated using 32 incident waves and has a 2% noise level. First column (a, d): true geometry. Second column (b, e): reconstruction with $k = 8$. Third column (c, f): reconstruction with $k = 16$.

2.2.2 Reconstruction with different numbers of incident waves (Figure 3)

We present the reconstruction results in Figure 3 for noisy data using 8 incident waves and 32 incident waves. The data is added with 20% noise and correspond to the wave number $k = 16$. It is clearly seen that the results significantly improve with an increased count of incident waves used to generate the data. However, it is worth noting that the results will remain relatively stable even as more incident waves are used in the reconstruction process.

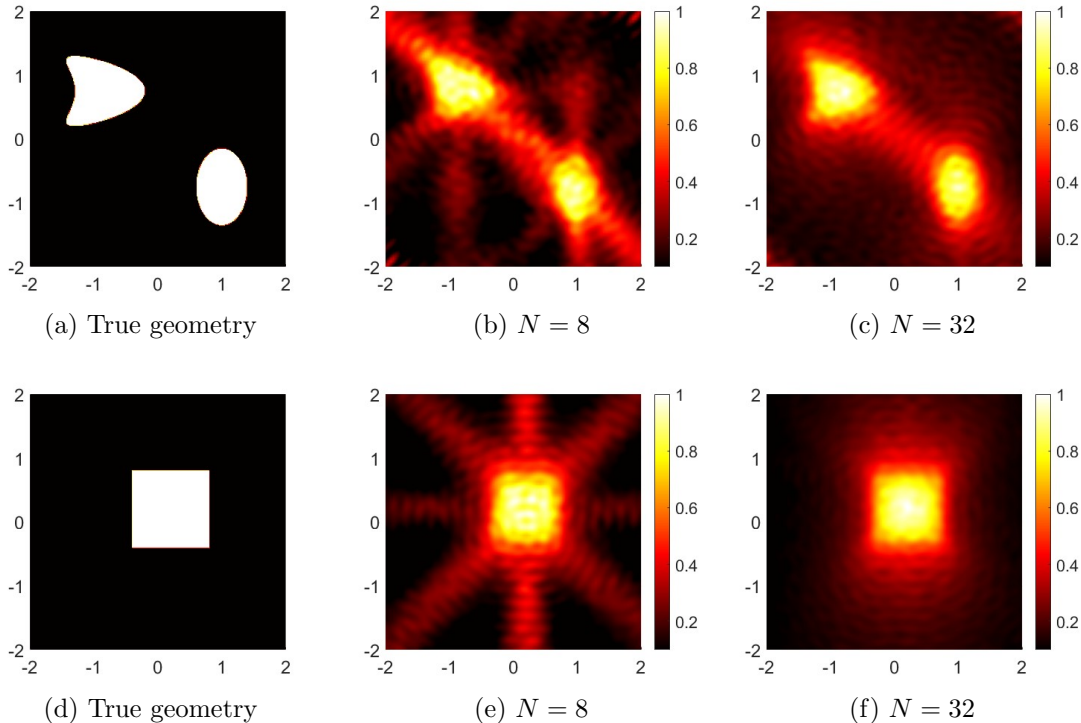


Figure 3: Reconstruction with noisy data using different numbers of incident waves. The wave number is $k = 16$ and the data is added by 20% noise. First column (a, d): true geometry. Second column (b, e): reconstruction using 8 incident waves ($N = 8$). Third column (c, f): reconstruction using 32 incident waves ($N = 32$).

2.2.3 Reconstruction with different powers p (Figure 4)

Figure 4 presents the reconstruction results using different values of p in $I(z)$. We consider a 20% noise level in the data, a wave number of $k = 16$, and again, 32 incident waves. While the reconstructions with $p = 1$ display reasonable locations and shapes of the targets, they are not as sharp or visually appealing as those in the case of $p = 2$ shown in Figure 3. The results with $p = 4$ are even less accurate in terms of the shape of the computed objects. These two experiments indicate that using $p = 2$ seems to yield the most reasonable results.

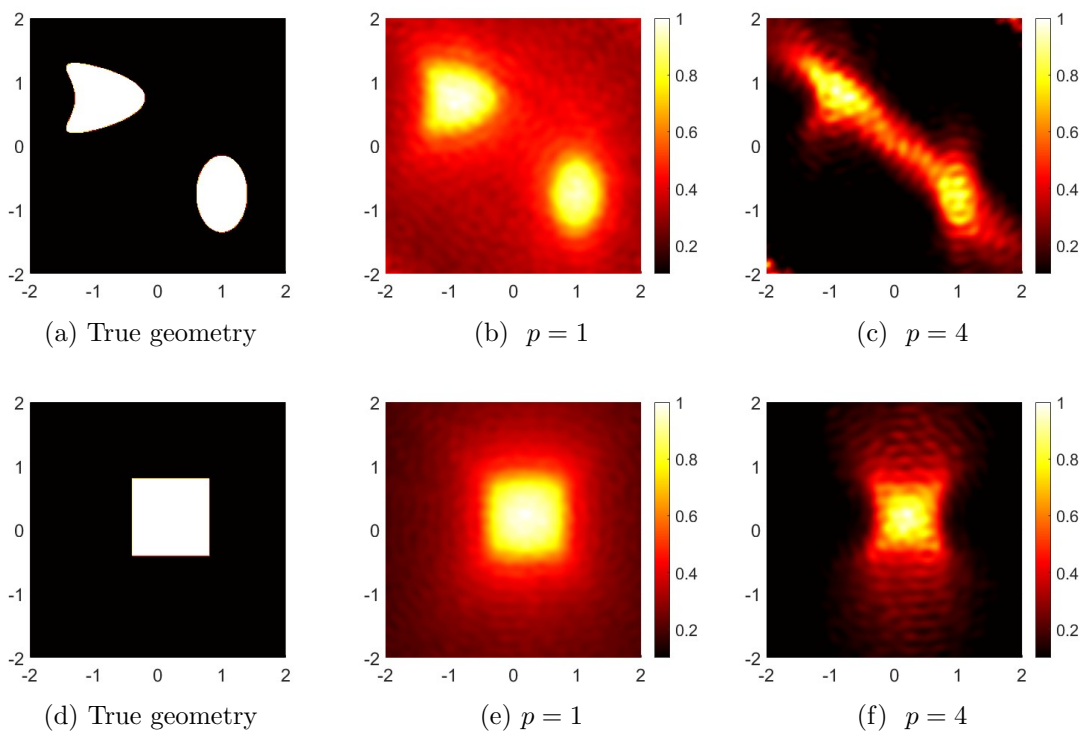


Figure 4: Reconstruction with noisy data (20% noise) using different values of p , 32 incident waves, wave number $k = 16$. First column (a, d): true geometry. Second column (b, e): reconstruction with $p = 1$. Third column (c, f): reconstruction with $p = 4$.

3 The Case of Maxwell's Equations

We consider the scattering of time-harmonic electromagnetic waves at positive wave number k from a non-magnetic inhomogeneous medium. Suppose that there is no free charge and current density. Then, the electric field \mathbf{E} and the magnetic field \mathbf{H} satisfy the Maxwell's equations

$$\operatorname{curl} \mathbf{E} - ik\mathbf{H} = 0 \quad \text{and} \quad \operatorname{curl} \mathbf{H} + ik\varepsilon\mathbf{E} = 0 \quad \text{in } \mathbb{R}^3, \quad (13)$$

where ε is the electric permittivity of the medium (the magnetic permeability is assumed to be 1). The permittivity ε is assumed to be a bounded matrix-valued function. Let D be a bounded domain occupied by the non-magnetic inhomogeneous medium. The medium outside D is assumed to be homogeneous which means $\varepsilon = I_3$ outside D . Eliminating magnetic field \mathbf{H} from (13) we obtain

$$\operatorname{curl} \operatorname{curl} \mathbf{E} - k^2\varepsilon\mathbf{E} = 0, \quad \text{in } \mathbb{R}^3. \quad (14)$$

Assume that the inhomogeneous medium is illuminated by the incident electric and magnetic incident fields \mathbf{E}_{in} and \mathbf{H}_{in} , respectively, satisfying

$$\operatorname{curl} \mathbf{H}_{\text{in}} + ik\mathbf{E}_{\text{in}} = 0 \quad \text{and} \quad \operatorname{curl} \mathbf{E}_{\text{in}} - ik\mathbf{H}_{\text{in}} = 0, \quad \text{in } \mathbb{R}^3.$$

Then there arises the scattered electric field \mathbf{u} , defined by $\mathbf{u} := \mathbf{E} - \mathbf{E}_{\text{in}}$. Since the incident field \mathbf{E}_{in} satisfies the homogeneous Maxwell equation with wave number k given by

$$\text{curl curl } \mathbf{E}_{\text{in}} - k^2 \mathbf{E}_{\text{in}} = 0, \quad \text{in } \mathbb{R}^3$$

subtracting this equation from (14) we can conclude that the scattered field satisfies

$$\text{curl curl } \mathbf{u} - k^2 \varepsilon \mathbf{u} = k^2 P \mathbf{E}_{\text{in}} \quad \text{in } \mathbb{R}^3, \quad (15)$$

where the contrast P is defined by

$$P := \varepsilon - I_3.$$

Therefore, $P = 0$ in $\mathbb{R}^3 \setminus \overline{D}$. We complete the scattering problem by the Silver-Müller radiation condition for the scattered field \mathbf{u} given by

$$\frac{\mathbf{x}}{|\mathbf{x}|} \times \text{curl } \mathbf{u} - ik\mathbf{u} = \mathcal{O}(|\mathbf{x}|^{-2}) \quad \text{as } |\mathbf{x}| \rightarrow \infty, \quad (16)$$

which is assumed to hold uniformly with respect to $\mathbf{x}/|\mathbf{x}|$. For the study of the inverse problem discussed below we assume that the problem (15)–(16) is well-posed. The well-posedness of this direct problem was studied in [18].

Let Ω be a regular domain such that $\overline{D} \subset \Omega$ and ν be the outward normal unit on $\partial\Omega$. Consider N incident fields \mathbf{E}_{in} as plane waves

$$\mathbf{E}_{\text{in}}(\mathbf{x}, \mathbf{d}_j) = \mathbf{q}_j e^{ik\mathbf{d}_j \cdot \mathbf{x}}, \quad \mathbf{d}_j \in \mathbb{S}^2, \quad j = 1, \dots, N,$$

where \mathbf{q}_j is the polarization vector in \mathbb{R}^3 that is orthogonal to \mathbf{d}_j . We consider the following inverse problem.

Inverse problem. Given $\mathbf{u}(\cdot, \mathbf{d}_j)$ and $\nu \times \text{curl } \mathbf{u}(\cdot, \mathbf{d}_j)$ on $\partial\Omega$ for $\mathbf{d}_j \in \mathbb{S}^2$ where $j = 1, \dots, N$, determine D .

Remark 5. From Maxwell equations (13), it is evident that the data \mathbf{u} and $\nu \times \text{curl } \mathbf{u}$ can be respectively obtained through the measurement of the electric field \mathbf{E} and the tangential components of the magnetic field, $\nu \times \mathbf{H}$, on $\partial\Omega$.

Similar to the scalar case, an integro-differential equation formulation for the scattered field \mathbf{u} is needed to investigate the imaging functional. To this end, we need the Green's tensor of the scattering problem (15)–(16) that is given by

$$\mathbb{G}(\mathbf{x}, \mathbf{y}) = \Phi(\mathbf{x}, \mathbf{y}) I_3 + \frac{1}{k^2} \nabla_{\mathbf{x}} \text{div}_{\mathbf{x}} (\Phi(\mathbf{x}, \mathbf{y}) I_3), \quad \mathbf{x} \neq \mathbf{y}, \quad (17)$$

where

$$\Phi(\mathbf{x}, \mathbf{y}) = \frac{e^{ik|\mathbf{x}-\mathbf{y}|}}{4\pi|\mathbf{x}-\mathbf{y}|}.$$

It is known from [18] that the scattered field \mathbf{u} (weak solution in $H_{\text{loc}}(\text{curl}, \mathbb{R}^3)$) in problem (15)–(16) can be described by the following the integro-differential equation

$$\mathbf{u}(\mathbf{x}) = (k^2 + \nabla \text{div}) \int_D \Phi(\mathbf{x}, \mathbf{y}) P(\mathbf{y}) \mathbf{E}(\mathbf{y}) d\mathbf{y}, \quad \mathbf{x} \in \mathbb{R}^3. \quad (18)$$

3.1 Stable Imaging Functional

Let \mathbf{p}_n be vectors in \mathbb{S}^2 , $n = 1, 2, \dots, M$. We define the imaging functional

$$\mathcal{I}(\mathbf{z}) := \sum_{n=1}^M \sum_{j=1}^N \left| \int_{\partial\Omega} [\nu \times \text{curl}(\text{Im } \mathbb{G}(\mathbf{x}, \mathbf{z})\mathbf{p}_n)] \cdot \mathbf{u}(\mathbf{x}, \mathbf{d}_j) - \text{Im } \mathbb{G}(\mathbf{x}, \mathbf{z})\mathbf{p}_n \cdot [\nu \times \text{curl } \mathbf{u}(\mathbf{x}, \mathbf{d}_j)] \, ds(\mathbf{x}) \right|^p, \quad (19)$$

where $\mathbf{z} \in \mathbb{R}^3$ and $p \in \mathbb{N}$ is again used to sharpen the significant peaks of $\mathcal{I}(\mathbf{z})$.

Remark 6. *Based on numerical observations of the kernel function $\mathcal{K}(\mathbf{y}, \mathbf{z}, \mathbf{p}_n)$ in (21) (see Figure 5) and the numerical study of the imaging functional (see Figure 8), using multiple vectors \mathbf{p}_n tends to yield improved reconstruction results. Moreover, similar to the scalar case, when the measurements are acquired along the boundary of a large-radius ball, utilizing the radiation condition allows us to approximate $\nu \times \text{curl } \mathbf{u}$ by $ik\mathbf{u}$ in (19).*

Recall that j_0 is the spherical Bessel function of the first kind. We study the behavior of the imaging functional $\mathcal{I}(\mathbf{z})$ in the following theorem.

Theorem 7. *The imaging functional satisfies*

$$\mathcal{I}(\mathbf{z}) = \sum_{n=1}^M \sum_{j=1}^N \left| \int_D \mathcal{K}(\mathbf{y}, \mathbf{z}, \mathbf{p}_n) \cdot P(\mathbf{y})\mathbf{E}(\mathbf{y}, \mathbf{d}_j) \, d\mathbf{y} \right|^p, \quad (20)$$

where

$$\begin{aligned} \mathcal{K}(\mathbf{y}, \mathbf{z}, \mathbf{p}_n) = & -\frac{k\mathbf{p}_n|\mathbf{y} - \mathbf{z}|^2 - k(\mathbf{p}_n \cdot (\mathbf{y} - \mathbf{z}))(\mathbf{y} - \mathbf{z})}{4\pi|\mathbf{y} - \mathbf{z}|^2} j_0(k|\mathbf{y} - \mathbf{z}|) \\ & + \frac{3(\mathbf{p}_n \cdot (\mathbf{y} - \mathbf{z}))(\mathbf{y} - \mathbf{z}) - \mathbf{p}_n|\mathbf{y} - \mathbf{z}|^2}{k4\pi|\mathbf{y} - \mathbf{z}|^4} (\cos(k|\mathbf{y} - \mathbf{z}|) - j_0(k|\mathbf{y} - \mathbf{z}|)). \end{aligned} \quad (21)$$

Furthermore

$$\mathcal{I}(\mathbf{z}) = O\left(\frac{1}{\text{dist}(\mathbf{z}, D)^p}\right) \quad \text{as } \text{dist}(\mathbf{z}, D) \rightarrow \infty. \quad (22)$$

Remark 8. *Similar to the scalar case, the kernel $\mathcal{K}(\mathbf{y}, \mathbf{z}, \mathbf{p}_n)$ exhibits the desired peak property in magnitude which partially explain the behavior of $\mathcal{I}(\mathbf{z})$. The peak of the kernel in this case is even better than that of the scalar case, as seen in Figure 5. Moreover, the summation of $|\mathcal{K}(\mathbf{y}, \mathbf{z}, \mathbf{p}_n)|^2$ over multiple vectors \mathbf{p}_n results in a stronger and more rounded peak, potentially enhancing the performance of the imaging functional. This observation is confirmed in the numerical study.*

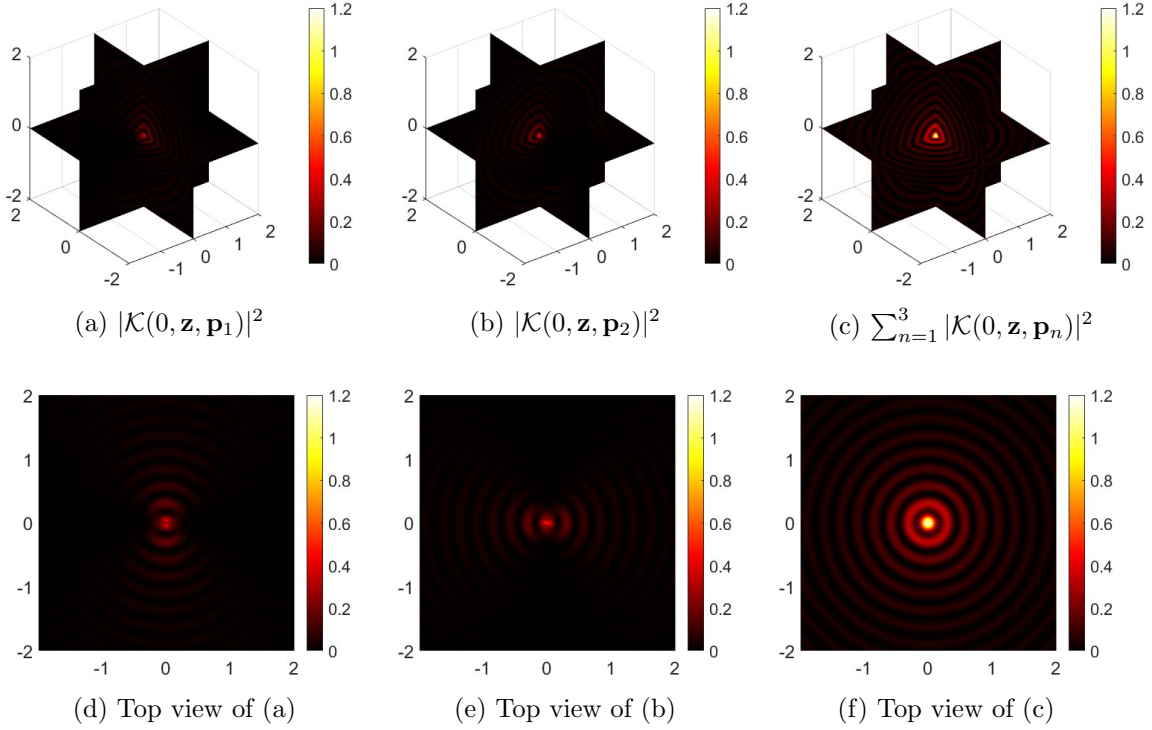


Figure 5: Plots illustrating $|\mathcal{K}(\mathbf{y}, \mathbf{z}, \mathbf{p}_1)|^2$, $|\mathcal{K}(\mathbf{y}, \mathbf{z}, \mathbf{p}_2)|^2$, and $\sum_{n=1}^3 |\mathcal{K}(\mathbf{y}, \mathbf{z}, \mathbf{p}_n)|^2$, respectively, in (a), (b), and (c), for $\mathbf{y} = 0$, $\mathbf{z} \in (-2, 2)^2$, $k = 12$, and $\mathbf{p}_1 = (1, 0, 0)^\top$, $\mathbf{p}_2 = (0, 1, 0)^\top$, $\mathbf{p}_3 = (0, 0, 1)^\top$.

Proof. From (18) and a direct calculation we obtain

$$\begin{aligned} \mathbf{u}(\mathbf{x}) &= \int_D \mathbb{G}(\mathbf{x}, \mathbf{y}) P(\mathbf{y}) \mathbf{E}(\mathbf{y}) d\mathbf{y}, \\ \nu \times \text{curl } \mathbf{u}(\mathbf{x}) &= \int_D \nu \times \text{curl}_{\mathbf{x}} (\mathbb{G}(\mathbf{x}, \mathbf{y})) P(\mathbf{y}) \mathbf{E}(\mathbf{y}) d\mathbf{y}, \end{aligned}$$

where curl of the Green's tensor is taken columnwise. A substitution leads to

$$\begin{aligned} & \int_{\partial\Omega} [\nu \times \text{curl} (\text{Im } \mathbb{G}(\mathbf{x}, \mathbf{z}) \mathbf{p}_n)] \cdot \mathbf{u}(\mathbf{x}, \mathbf{d}_j) - \text{Im } \mathbb{G}(\mathbf{x}, \mathbf{z}) \mathbf{p}_n \cdot [\nu \times \text{curl } \mathbf{u}(\mathbf{x}, \mathbf{d}_j)] ds(x) \\ &= \int_{\partial\Omega} [\nu \times \text{curl} (\text{Im } \mathbb{G}(\mathbf{x}, \mathbf{z}) \mathbf{p}_n)] \cdot \int_D \mathbb{G}(\mathbf{x}, \mathbf{y}) P(\mathbf{y}) \mathbf{E}(\mathbf{y}) d\mathbf{y} \\ & \quad - \text{Im } \mathbb{G}(\mathbf{x}, \mathbf{z}) \mathbf{p}_n \cdot \left[\int_D \nu \times \text{curl}_{\mathbf{x}} [\mathbb{G}(\mathbf{x}, \mathbf{y})] P(\mathbf{y}) \mathbf{E}(\mathbf{y}) d\mathbf{y} \right] ds(x) \\ &= \int_D \int_{\partial\Omega} [\nu \times \text{curl} (\text{Im } \mathbb{G}(\mathbf{x}, \mathbf{z}) \mathbf{p}_n)] \cdot \mathbb{G}(\mathbf{x}, \mathbf{y}) P(\mathbf{y}) \mathbf{E}(\mathbf{y}) \\ & \quad - \text{Im } \mathbb{G}(\mathbf{x}, \mathbf{z}) \mathbf{p}_n \cdot [\nu \times \text{curl}_{\mathbf{x}} (\mathbb{G}(\mathbf{x}, \mathbf{y})) P(\mathbf{y}) \mathbf{E}(\mathbf{y})] ds(x) d\mathbf{y}. \end{aligned} \tag{23}$$

Now we will compute the integral over $\partial\Omega$ in the equation (23). First from (17) and a direct calculation we have that

$$\operatorname{Im} \mathbb{G}(\mathbf{x}, \mathbf{z})\mathbf{p}_n = \operatorname{Im} \Phi(\mathbf{x}, \mathbf{z})\mathbf{p}_n + \frac{1}{k^2} \nabla_{\mathbf{x}} \operatorname{div}_{\mathbf{x}}(\operatorname{Im} \Phi(\mathbf{x}, \mathbf{z})\mathbf{p}_n).$$

Using this result, the identities $\operatorname{curl} \nabla = 0$, $\operatorname{curl} \operatorname{curl} = -\Delta + \nabla \operatorname{div}$, and the fact that

$$\Delta_{\mathbf{x}} \operatorname{Im} \Phi(\mathbf{x}, \mathbf{z}) = -k^2 \operatorname{Im} \Phi(\mathbf{x}, \mathbf{z}), \quad \text{for all } \mathbf{x}, \mathbf{z} \in \mathbb{R}^3,$$

we derive

$$\operatorname{curl}_{\mathbf{x}} \operatorname{curl}_{\mathbf{x}} (\operatorname{Im} \mathbb{G}(\mathbf{x}, \mathbf{z})\mathbf{p}_n) = k^2 \operatorname{Im} \mathbb{G}(\mathbf{x}, \mathbf{z})\mathbf{p}_n \quad \text{for all } \mathbf{x}, \mathbf{z} \in \mathbb{R}^3. \quad (24)$$

In addition, for $\mathbf{q} \in \mathbb{R}^3$, we have

$$\operatorname{curl}_{\mathbf{x}} \operatorname{curl}_{\mathbf{x}} (\mathbb{G}(\mathbf{x}, \mathbf{y})\mathbf{q}) - k^2 \mathbb{G}(\mathbf{x}, \mathbf{y})\mathbf{q} = -\delta(\mathbf{x} - \mathbf{y})\mathbf{q}. \quad (25)$$

Multiplying equations (25) and (24) by $\operatorname{Im} \mathbb{G}(\mathbf{x}, \mathbf{z})\mathbf{p}_n$ and $\mathbb{G}(\mathbf{x}, \mathbf{y})\mathbf{q}$, respectively, and integrating over Ω we obtain

$$\begin{aligned} \int_{\Omega} \operatorname{curl}_{\mathbf{x}} \operatorname{curl}_{\mathbf{x}} (\mathbb{G}(\mathbf{x}, \mathbf{y})\mathbf{q}) \cdot \operatorname{Im} \mathbb{G}(\mathbf{x}, \mathbf{z})\mathbf{p}_n - k^2 \mathbb{G}(\mathbf{x}, \mathbf{y})\mathbf{q} \cdot \operatorname{Im} \mathbb{G}(\mathbf{x}, \mathbf{z})\mathbf{p}_n \, d\mathbf{x} &= -\mathbf{q} \cdot \operatorname{Im} \mathbb{G}(\mathbf{y}, \mathbf{z})\mathbf{p}_n, \\ \int_{\Omega} \operatorname{curl}_{\mathbf{x}} \operatorname{curl}_{\mathbf{x}} (\operatorname{Im} \mathbb{G}(\mathbf{x}, \mathbf{z})\mathbf{p}_n) \cdot \mathbb{G}(\mathbf{x}, \mathbf{y})\mathbf{q} - k^2 \operatorname{Im} \mathbb{G}(\mathbf{x}, \mathbf{z})\mathbf{p}_n \cdot \mathbb{G}(\mathbf{x}, \mathbf{y})\mathbf{q} \, d\mathbf{x} &= 0. \end{aligned}$$

Making a subtraction of the two equations above and integrating by parts we derive

$$\begin{aligned} \int_{\partial\Omega} \operatorname{Im} \mathbb{G}(\mathbf{x}, \mathbf{z})\mathbf{p}_n \cdot \nu \times \operatorname{curl}_{\mathbf{x}} \mathbb{G}(\mathbf{x}, \mathbf{y})\mathbf{q} - \nu \times \operatorname{curl}_{\mathbf{x}} \operatorname{Im} \mathbb{G}(\mathbf{x}, \mathbf{z})\mathbf{p}_n \cdot \mathbb{G}(\mathbf{x}, \mathbf{y})\mathbf{q} \, ds(\mathbf{x}) \\ = -\mathbf{q} \cdot \operatorname{Im} \mathbb{G}(\mathbf{y}, \mathbf{z})\mathbf{p}_n. \end{aligned}$$

Choosing $\mathbf{q} = P(\mathbf{y})\mathbf{E}(\mathbf{y})$ leads to

$$\begin{aligned} \int_{\partial\Omega} \operatorname{Im} \mathbb{G}(\mathbf{x}, \mathbf{z})\mathbf{p}_n \cdot \nu \times \operatorname{curl}_{\mathbf{x}} \mathbb{G}(\mathbf{x}, \mathbf{y})P(\mathbf{y})\mathbf{E}(\mathbf{y}) - \nu \times \operatorname{curl}_{\mathbf{x}} \operatorname{Im} \mathbb{G}(\mathbf{x}, \mathbf{z})\mathbf{p}_n \cdot \mathbb{G}(\mathbf{x}, \mathbf{y})P(\mathbf{y})\mathbf{E}(\mathbf{y}) \, ds(\mathbf{x}) \\ = -P(\mathbf{y})\mathbf{E}(\mathbf{y}) \cdot \operatorname{Im} \mathbb{G}(\mathbf{y}, \mathbf{z})\mathbf{p}_n. \end{aligned}$$

Now substituting this result in (23) and comparing with $\mathcal{I}(\mathbf{z})$ given in (19) we obtain

$$\mathcal{I}(\mathbf{z}) = \sum_{n=1}^M \sum_{j=1}^N \left| \int_D \operatorname{Im} \mathbb{G}(\mathbf{y}, \mathbf{z})\mathbf{p}_n \cdot P(\mathbf{y})\mathbf{E}(\mathbf{y}) \, d\mathbf{y} \right|^p.$$

Setting $\mathcal{K}(\mathbf{y}, \mathbf{z}, \mathbf{p}_n) = \operatorname{Im} \mathbb{G}(\mathbf{y}, \mathbf{z})\mathbf{p}_n$ then

$$\mathcal{K}(\mathbf{y}, \mathbf{z}, \mathbf{p}_n) = \frac{k}{4\pi} \left(j_0(k|\mathbf{y} - \mathbf{z}|)\mathbf{p}_n + \frac{1}{k^2} \nabla_{\mathbf{y}} \operatorname{div}_{\mathbf{y}}(j_0(k|\mathbf{y} - \mathbf{z}|)\mathbf{p}_n) \right).$$

Recall that $j_0(k|\mathbf{y} - \mathbf{z}|) = \sin(k|\mathbf{y} - \mathbf{z}|)/(k|\mathbf{y} - \mathbf{z}|)$, a straightforward calculation implies

$$\begin{aligned} \mathcal{K}(\mathbf{y}, \mathbf{z}, \mathbf{p}_n) &= -\frac{k\mathbf{p}_n|\mathbf{y} - \mathbf{z}|^2 - k(\mathbf{p}_n \cdot (\mathbf{y} - \mathbf{z}))(\mathbf{y} - \mathbf{z})}{4\pi|\mathbf{y} - \mathbf{z}|^2} j_0(k|\mathbf{y} - \mathbf{z}|) \\ &\quad + \frac{3(\mathbf{p}_n \cdot (\mathbf{y} - \mathbf{z}))(\mathbf{y} - \mathbf{z}) - \mathbf{p}_n|\mathbf{y} - \mathbf{z}|^2}{k4\pi|\mathbf{y} - \mathbf{z}|^4} (\cos(k|\mathbf{y} - \mathbf{z}|) - j_0(k|\mathbf{y} - \mathbf{z}|)). \end{aligned}$$

Using the Cauchy-Schwartz and triangle inequalities we obtain

$$|\mathcal{K}(\mathbf{y}, \mathbf{z}, \mathbf{p}_n)| \leq \frac{k}{2\pi} |j_0(k|\mathbf{y} - \mathbf{z}|)| + \frac{1 + |j_0(k|\mathbf{y} - \mathbf{z}|)|}{k\pi|\mathbf{y} - \mathbf{z}|}.$$

From this estimate and the fact that $j_0(k|\mathbf{y} - \mathbf{z}|) = O(1/|\mathbf{y} - \mathbf{z}|)$ as $|\mathbf{y} - \mathbf{z}| \rightarrow \infty$ we imply that

$$|\mathcal{K}(\mathbf{y}, \mathbf{z}, \mathbf{p}_n)| = O\left(\frac{1}{|\mathbf{y} - \mathbf{z}|}\right), \quad \text{as } |\mathbf{y} - \mathbf{z}| \rightarrow \infty,$$

which can help us deduce (22) similarly as in the scalar case. □

We assume the noisy data \mathbf{u}^δ and $\nu \times \text{curl } \mathbf{u}^\delta$ satisfy

$$\begin{aligned} \sum_{j=1}^N \|\mathbf{u}(\cdot, \mathbf{d}_j) - \mathbf{u}^\delta(\cdot, \mathbf{d}_j)\|_{(L^2(\partial\Omega))^3} &\leq \delta_1, \\ \sum_{j=1}^N \|\nu \times \text{curl } \mathbf{u}(\cdot, \mathbf{d}_j) - \nu \times \text{curl } \mathbf{u}^\delta(\cdot, \mathbf{d}_j)\|_{(L^2(\partial\Omega))^3} &\leq \delta_2, \end{aligned}$$

for some positive constants δ_1, δ_2 . We now have a stability estimate for the imaging functional $\mathcal{I}(\mathbf{z})$.

Theorem 9. *Denote by $\mathcal{I}^\delta(\mathbf{z})$ the imaging functional corresponding to noisy data \mathbf{u}^δ and $\nu \times \text{curl } \mathbf{u}^\delta$, that means,*

$$\mathcal{I}^\delta(\mathbf{z}) = \sum_{n=1}^M \sum_{j=1}^N \left| \int_{\partial\Omega} [\nu \times \text{curl}(\text{Im } \mathbb{G}(\mathbf{x}, \mathbf{z})\mathbf{p}_n)] \cdot \mathbf{u}^\delta(\mathbf{x}, \mathbf{d}_j) - \text{Im } \mathbb{G}(\mathbf{x}, \mathbf{z})\mathbf{p}_n \cdot [\nu \times \text{curl } \mathbf{u}^\delta(\mathbf{x}, \mathbf{d}_j)] \, ds(x) \right|^p.$$

Then for all $\mathbf{z} \in \mathbb{R}^3$,

$$|\mathcal{I}(\mathbf{z}) - \mathcal{I}^\delta(\mathbf{z})| = O(\max\{\delta_1, \delta_2\}) \quad \text{as } \max\{\delta_1, \delta_2\} \rightarrow 0.$$

Proof. The proof can be done similarly as in the scalar case and is therefore omitted. □

3.2 Numerical Examples

We provide numerical examples to effectively illustrate the efficiency of the imaging functional $\mathcal{I}(\mathbf{z})$ in reconstructing scatterers using simulated data. Specifically, we examine the performance of the functional using different numbers of incident waves (Figure 7), using different sets of vectors \mathbf{p}_n for $n = 1, \dots, M$ (Figure 8), and using highly noisy data (Figure 6). As in the scalar case, the imaging functional is normalized by dividing it with its maximal value.

The following common parameters are used in the numerical examples

$$\begin{aligned} \partial\Omega &= \{(x_1, x_2, x_3)^\top \in \mathbb{R}^3 : x_1^2 + x_2^2 + x_3^2 = 3^2\}, \\ \text{Number of data points on } \partial\Omega &: 324 \text{ (uniformly distributed)}, \\ \text{Sampling domain} &: (-1.5, 1.5)^3, \\ \text{Number of sampling points} &: 60^3, \\ \text{Power } p \text{ in } I(z) &: p = 2, \\ \text{Isovalue for 3D plots in Matlab} &: 0.4. \end{aligned}$$

The choice of $p = 2$ follows from the numerical study in the 2D case. The following scattering object consisting a sphere (D_1) and an L shape ($D_2 \setminus D_3$) is considered in the numerical examples in Figures 7–6

$$\begin{aligned} D_1 &= \{\mathbf{x} \in \mathbb{R}^3 : |\mathbf{x} - \mathbf{a}|^2 < 0.5^2, \mathbf{a} = (0.6, 0, 0.5)^\top\}, \\ D_2 &= \{\mathbf{x} \in \mathbb{R}^3 : -1.1 < x_1 < 0.1, -0.3 < x_2 < 0.3, -1 < x_3 < 0.2\}, \\ D_3 &= \{\mathbf{x} \in \mathbb{R}^3 : -0.5 < x_1 < 0.1, -0.3 < x_2 < 0.3, -0.4 < x_3 < 0.2\}, \\ Q(\mathbf{x}) &= \begin{cases} \text{diag}(0.5, 0.4, 0.3), & \mathbf{x} \in D_1 \cup (D_2 \setminus \overline{D_3}) \\ 0, & \text{else.} \end{cases} \end{aligned}$$

We consider the incident plane waves

$$\mathbf{E}_{\text{in}}(\mathbf{x}, \mathbf{d}_j) = (\mathbf{d}_j \times (1, 0, 0)^\top) e^{ik\mathbf{d}_j \cdot \mathbf{x}}, \quad \mathbf{d}_j \in \mathbb{S}^2, \quad j = 1, \dots, N,$$

where the wave vectors \mathbf{d}_j were generated almost uniformly on \mathbb{S}^2 . It was observed during the numerical study that the choice of using $(1, 0, 0)^\top$ in the polarization of $\mathbf{E}_{\text{in}}(\mathbf{x}, \mathbf{d}_j)$ or other vectors did not appear to significantly impact the reconstruction results. We simulated artificial noise using complex-valued noise matrices, similar to the approach used in the Helmholtz equation case.

3.2.1 Reconstruction with different wave numbers (Figure 6)

Figure 6 presents the reconstruction results for the wave numbers $k = 6$ (wavelength ≈ 1.04) and $k = 12$ (wavelength ≈ 0.52). We consider 180 incident waves to generate the data, which is perturbed by a 2% noise level ($\delta = 0.02$). As in the scalar case, we intentionally introduce a small amount of noise into the data to distinctly demonstrate the impact of using different wave numbers in the reconstruction process. Figure 6 illustrates that the reconstruction results notably improve with higher values of k .

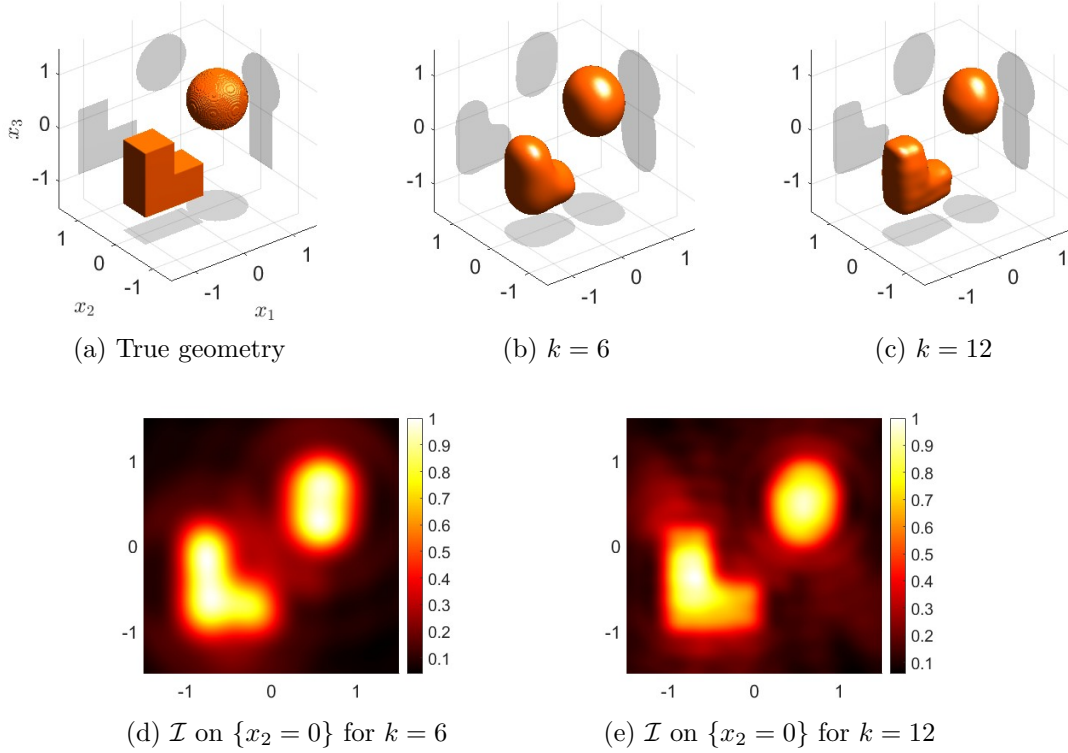


Figure 6: Reconstruction from data associated with different wave numbers. The data is generated using 180 incident waves and has a 2% noise level. $M = 3$ with $\mathbf{p}_1 = (1, 0, 0)^\top$, $\mathbf{p}_2 = (0, 1, 0)^\top$, $\mathbf{p}_3 = (0, 0, 1)^\top$. (a): true geometry. (b, d): reconstruction with $k = 6$. (c, e): reconstruction with $k = 12$.

3.2.2 Reconstruction with different numbers of incident waves (Figure 7)

We present the reconstruction results in Figure 7 for noisy data using 48, 96 and 180 incident waves. The data is added with 20% noise and correspond to the wave number $k = 12$. We consider $M = 3$ with the vectors $\mathbf{p}_1 = (1, 0, 0)^\top$, $\mathbf{p}_2 = (0, 1, 0)^\top$, $\mathbf{p}_3 = (0, 0, 1)^\top$. Remarkably, the reconstructions are already quite good when using 48 incident waves to generate the data. The results show a slight improvement with the use of more incident waves. Importantly, these results remain consistent even when more than 180 incident waves are employed in the reconstruction process.

3.2.3 Reconstruction with different sets of vectors \mathbf{p}_n (Figure 8)

We present the reconstruction results in Figure 8 for noisy data using different sets of vectors \mathbf{p}_n for $n = 1, 2, \dots, M$. The data is added with 20% noise and correspond to the wave number $k = 12$. We consider three following cases: $M = 1$ and $\mathbf{p}_1 = (0, 1, 0)^\top$, $M = 1$ and $\mathbf{p}_1 = (1/\sqrt{2}, 0, 1/\sqrt{2})^\top$, $M = 3$, and $\mathbf{p}_1 = (1/\sqrt{2}, 1/\sqrt{2}, 0)^\top$, $\mathbf{p}_2 = (0, 1/\sqrt{2}, 1/\sqrt{2})^\top$, $\mathbf{p}_3 = (1/\sqrt{2}, 0, 1/\sqrt{2})^\top$. For $M = 1$, the reconstructions using $\mathbf{p}_1 = (0, 1, 0)^\top$ and $\mathbf{p}_1 =$

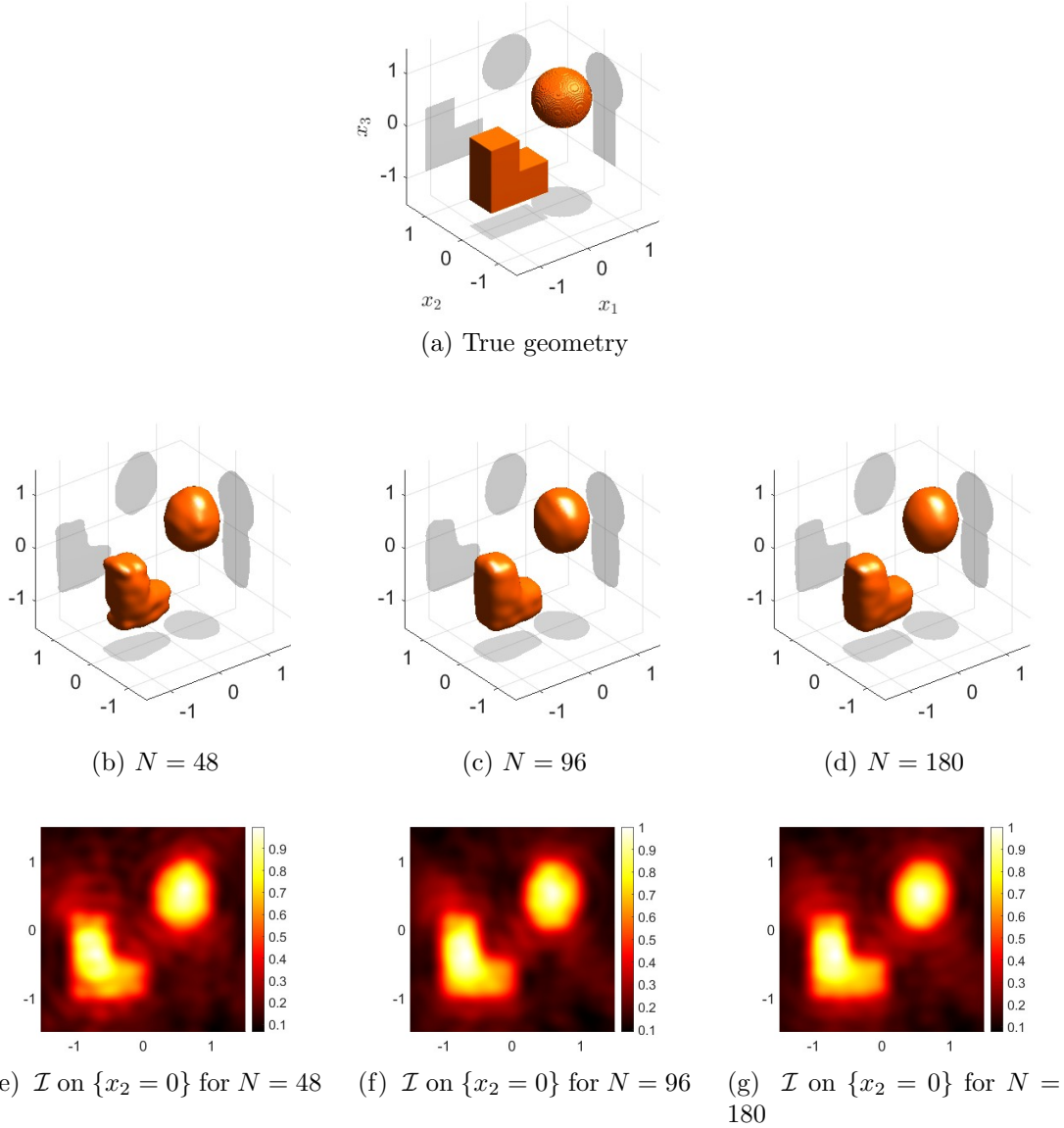


Figure 7: Reconstruction with noisy data (20% noise) using N incident waves, $k = 12$, and $M = 3$ with $\mathbf{p}_1 = (1, 0, 0)^\top$, $\mathbf{p}_2 = (0, 1, 0)^\top$, $\mathbf{p}_3 = (0, 0, 1)^\top$. First row (a): true geometry. (b, e): reconstruction with $N = 48$. (c, f): reconstruction with $N = 96$. (d, g): reconstruction with $N = 180$.

$(1/\sqrt{2}, 0, 1/\sqrt{2})^\top$ yield noticeably different results and are not as satisfactory as those obtained with $M = 3$. We also see that the result for $M = 3$ is similar to that of the case $M = 3$ and $\mathbf{p}_1 = (1, 0, 0)^\top$, $\mathbf{p}_2 = (0, 1, 0)^\top$, $\mathbf{p}_3 = (0, 0, 1)^\top$ presented in Figure 7. This aligns with the observation from Figure 5, where using more \mathbf{p}_n leads to improved peaks for the kernel function \mathcal{K} . Moreover, our numerical study supports the finding that employing $M = 3$ with three linearly independent vectors \mathbf{p}_n appears to provide the most reasonable and stable

results.

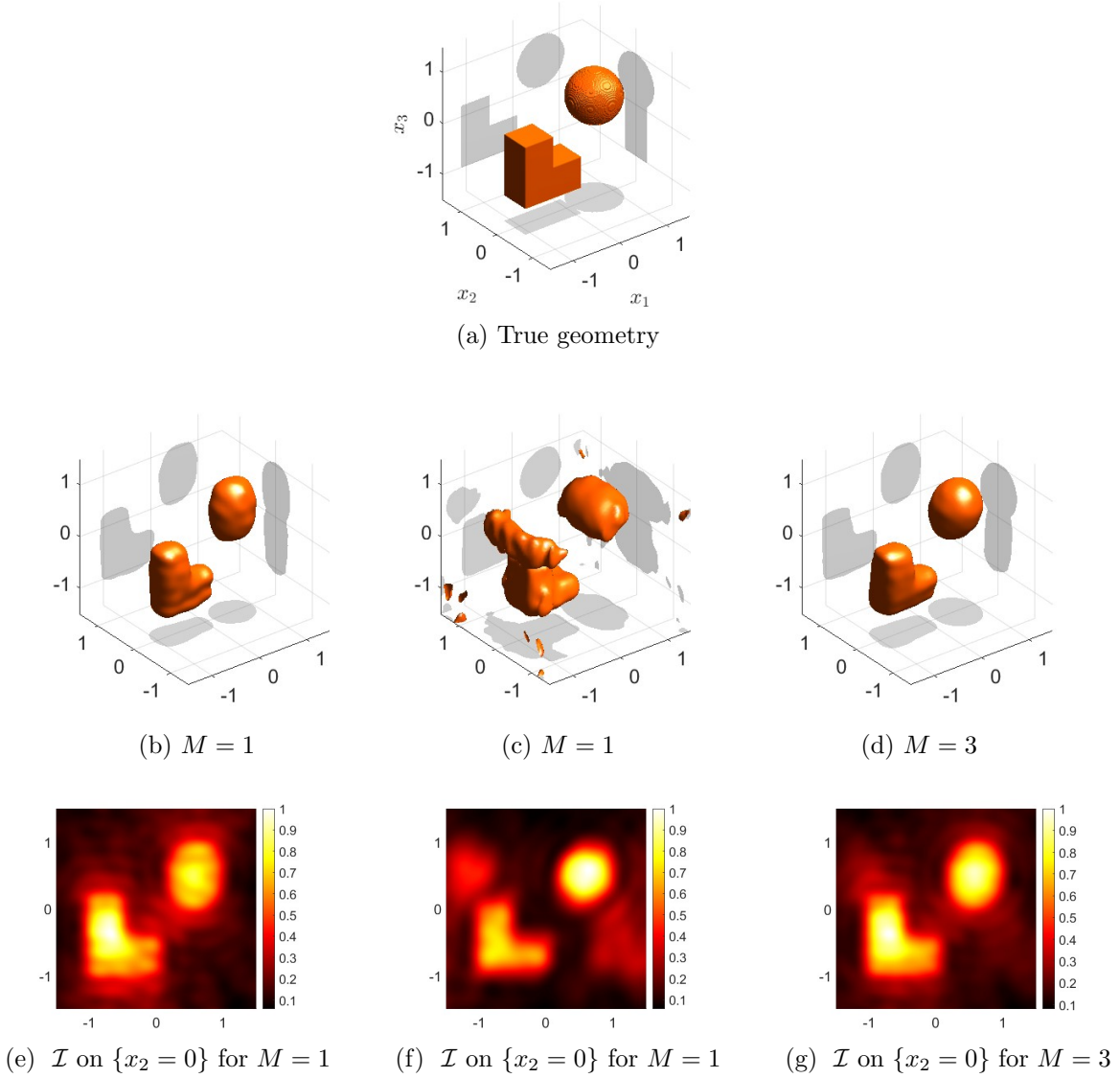


Figure 8: Reconstruction using different sets of vectors \mathbf{p}_n , $n = 1, 2, \dots, M$, $k = 12$, $N = 180$, and 20% noise in the data. (a): True geometry. (b, e): reconstruction with $M = 1$, $\mathbf{p}_1 = (0, 1, 0)^\top$. (c, f): reconstruction with $M = 1$, $\mathbf{p}_1 = (1/\sqrt{2}, 0, 1/\sqrt{2})^\top$. (d, g): reconstruction with $M = 3$, $\mathbf{p}_1 = (1/\sqrt{2}, 1/\sqrt{2}, 0)^\top$, $\mathbf{p}_2 = (0, 1/\sqrt{2}, 1/\sqrt{2})^\top$, $\mathbf{p}_3 = (1/\sqrt{2}, 0, 1/\sqrt{2})^\top$.

Acknowledgement. The first author acknowledges Ho Chi Minh City University of Technology and Education for funding her work through the grant No T2023-71. The work of the second author was partially supported by NSF grant DMS-2208293.

References

- [1] C. Y. Ahn, S. Chae, and W.-K. Park. Fast identification of short, sound-soft open arcs by the orthogonality sampling method in the limited-aperture inverse scattering problem. *Appl. Math. Lett.*, 109:106556, 2020.
- [2] M. Akinci, M. Cayoren, and I. Akduman. Near-field orthogonality sampling method for microwave imaging: Theory and experimental verification. *IEEE Trans. Microw. Theory Tech.*, 64:2489, 2016.
- [3] F. Cakoni and D. Colton. *Qualitative Methods in Inverse Scattering Theory. An Introduction*. Springer, Berlin, 2006.
- [4] F. Cakoni, D. Colton, and H. Haddar. *Inverse Scattering Theory and Transmission Eigenvalues*. SIAM, 2016.
- [5] F. Cakoni, D. Colton, and P. Monk. *The Linear Sampling Method in Inverse Electromagnetic Scattering*. SIAM, 2011.
- [6] D. Colton, H. Haddar, and M. Piana. The linear sampling method in inverse electromagnetic scattering theory. *Inverse Problems*, 19:S105–S137, 2003.
- [7] D. Colton and A. Kirsch. A simple method for solving inverse scattering problems in the resonance region. *Inverse Problems*, 12:383–393, 1996.
- [8] D. Colton and R. Kress. *Inverse Acoustic and Electromagnetic Scattering Theory*. Springer, New York, 3rd edition, 2013.
- [9] R. Griesmaier. Multi-frequency orthogonality sampling for inverse obstacle scattering problems. *Inverse Problems*, 27:085005, 2011.
- [10] I. Harris and A. Kleefeld. Analysis of new direct sampling indicators for far-field measurements. *Inverse Problems*, 35:054002, 2019.
- [11] I. Harris and D.-L. Nguyen. Orthogonality sampling method for the electromagnetic inverse scattering problem. *SIAM J. Sci. Comput.*, 42:B72–B737, 2020.
- [12] I. Harris, D.-L. Nguyen, and T.-P. Nguyen. Direct sampling methods for isotropic and anisotropic scatterers with point source measurements. *Inverse Probl. Imaging*, 16(5):1137–1162, 2022.
- [13] I. Harris and J. Rezac. A sparsity-constrained sampling method with applications to communications and inverse scattering. *J. Comput. Phys.*, 451:110890, 2022.
- [14] K. Ito, B. Jin, and J. Zou. A direct sampling method to an inverse medium scattering problem. *Inverse Problems*, 28:025003, 2012.

- [15] K. Ito, B. Jin, and J. Zou. A direct sampling method for inverse electromagnetic medium scattering. *Inverse Problems*, 29:095018, 2013.
- [16] S. Kang and M. Lambert. Structure analysis of direct sampling method in 3D electromagnetic inverse problem: near- and far-field configuration. *Inverse Problems*, 37:075002, 2021.
- [17] A. Kirsch. Characterization of the shape of a scattering obstacle using the spectral data of the far field operator. *Inverse Problems*, 14:1489–1512, 1998.
- [18] A. Kirsch. An integral equation approach and the interior transmission problem for Maxwell’s equations. *Inverse Probl. Imaging*, 1:159–180, 2007.
- [19] A. Kirsch. An integral equation for the scattering problem for an anisotropic medium and the Factorization method. In *8th int. workshop on mathematical methods in scattering theory and biomedical engineering*, 2007.
- [20] A. Kirsch and N.I. Grinberg. *The Factorization Method for Inverse Problems*. Oxford Lecture Series in Mathematics and its Applications 36. Oxford University Press, 2008.
- [21] T. Le, D.-L. Nguyen, V. Nguyen, and T. Truong. Sampling type method combined with deep learning for inverse scattering with one incident wave. *AMS Contemporary Mathematics*, 784:63–80, 2023.
- [22] T. Le, D.-L. Nguyen, H. Schmidt, and T. Truong. Imaging of 3D objects with experimental data using orthogonality sampling methods. *Inverse Problems*, 38:025007, 2022.
- [23] K. H. Leem, J. Liu, and G. Pelekanos. Two direct factorization methods for inverse scattering problems. *Inverse Problems*, 34:125004, 2018.
- [24] D.-L. Nguyen. Direct and inverse electromagnetic scattering problems for bi-anisotropic media. *Inverse Problems*, 35:124001, 2019.
- [25] W.-K. Park. Direct sampling method for retrieving small perfectly conducting cracks. *J. Comput. Phys.*, 373:648–661, 2018.
- [26] R. Potthast. A survey on sampling and probe methods for inverse problems. *Inverse Problems*, 22:R1–R47, 2006.
- [27] R. Potthast. A study on orthogonality sampling. *Inverse Problems*, 26:074015, 2010.